2.97-GHz CVD Diamond Ring Resonator With Q >40,000

Thura Lin Naing, Turker Beyazoglu, Lingqi Wu, Mehmet Akgul,
Zeying Ren, Tristan O. Rocheleau, and Clark T.-C. Nguyen
Dept. of Electrical Engineering and Computer Sciences
University of California at Berkeley
Berkeley, CA 94720 USA
E-mail: thura@eecs.berkeley.edu

***Abstract*— A capacitive-gap transduced micromechanical ring resonator based on a radial contour vibration mode and constructed from hot filament CVD boron-doped microcrystalline diamond has achieved a Q of 42,900 at 2.9685GHz that represents the highest series-resonant Q yet measured at this frequency for any on-chip room temperature resonator, as well as the highest $f{\cdot}Q$ of $1.27{\times}10^{14}$ for acoustic resonators, besting even macroscopic bulk-mode devices. Values like these in a device occupying only 870μm^2 may soon make possible on-chip realizations of RF channelizers and ultra-low phase-noise GHz oscillators for secure communications.**

***Keywords*—MEMS, CVD diamond, ring resonator, micromechanical, quality factor, resonator, oscillator, filter, RF MEMS.**

I. Introduction

Wireless communication receivers could be greatly simplified and improved if on-chip resonators with CAD-definable resonance frequencies in the GHz range and quality factors (Q's) over 30,000 were available to make possible RF channel-select filters and low phase noise oscillators. Such Q values could enable 0.1% or less bandwidth selectivity filters and unprecedented low phase noise oscillators, simultaneously improving the signal-to-noise ratio (SNR) of receivers and reducing the off-chip parts count. To elaborate, a typical receiver, as shown in Fig. 1, consists of a band-select filter, a low noise amplifier (LNA), and a mixer. If there were a high power in-band interferer close to the receiver, the output of the LNA would contain this in-band interferer in addition to the (lower-power) desired signal. The mixer multiplies—in the time domain—both signals with the output power of a local reference (LO) oscillator. If the phase noise of the LO oscillator is large enough, noise convoluted onto the interferer would then overshadow the desired signal, making it difficult to detect.

Clearly, the lower the LO phase noise, the higher the SNR at the mixer output. The phase noise of a linearly amplitude-level controlled oscillator possessing (for simplicity) only thermal noise can be described approximately by Leeson's equation [1]

$$\mathcal{L}(f) \cong 10\log\left[\frac{2FkT}{P_{sig}}\left(1+\frac{1}{Q^2}\left(\frac{f_o}{2\Delta f}\right)^2\right)\right] \qquad (1)$$

Much of the described work was supported by DARPA.

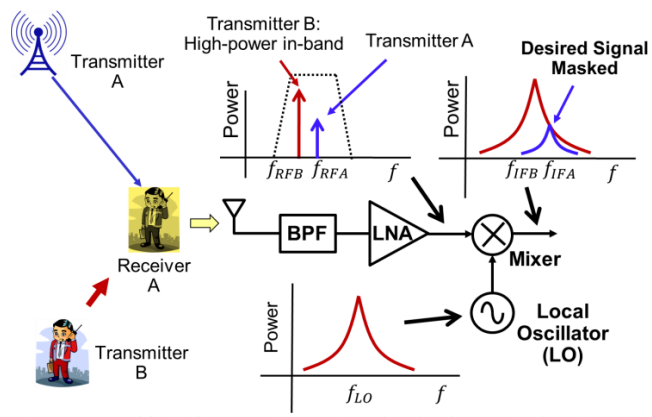

Fig. 1: System block diagram of a receiver showing how an in-band interferer can mask the desired signal if the phase noise of the LO is high.

where k and T are the Boltzmann constant and temperature, respectively, F is the amplifier noise figure, P_{sig} is the loop signal power, and Δf is the offset frequency from the oscillation frequency f_0. Equation (1) shows that phase noise decreases 1) linearly with decreasing noise; 2) linearly with increasing loop signal power, which is in turn governed by linearity; and 3) quadratically with increasing Q.

Given the above, it is not surprising that much effort has been spent over decades to realize resonators that achieve high Q, especially at high frequencies, e.g., GHz. To date, HBAR devices have long held the highest frequency-Q ($f{\cdot}Q$) products, with reported values as high as $1.10{\times}10^{14}$ [2] and $6.69{\times}10^{13}$ [3]. However, because these devices are generally overmoded, they must be used in tandem with at least one other filter that selects the desired mode frequency. If this is not desirable, then among non-overmoded devices, capacitive-gap transduced resonators have generally posted the highest Q's. In particular, capacitive-gap transduced ring resonators supported by symmetric and balanced quarter wavelength spoke beams to reduce anchor loss have achieved simultaneous high frequency and Q in polysilicon material, with Q's greater than 14,000 at 1.2GHz [4].

Pursuant to further raising Q's at GHz frequencies, this work harnesses the low (predicted) fundamental phonon scatter rate of diamond versus silicon [5][6] by replacing the previous polysilicon material used in the spoke-supported

978-1-4577-1820-5/12/$26.00 ©2012 IEEE

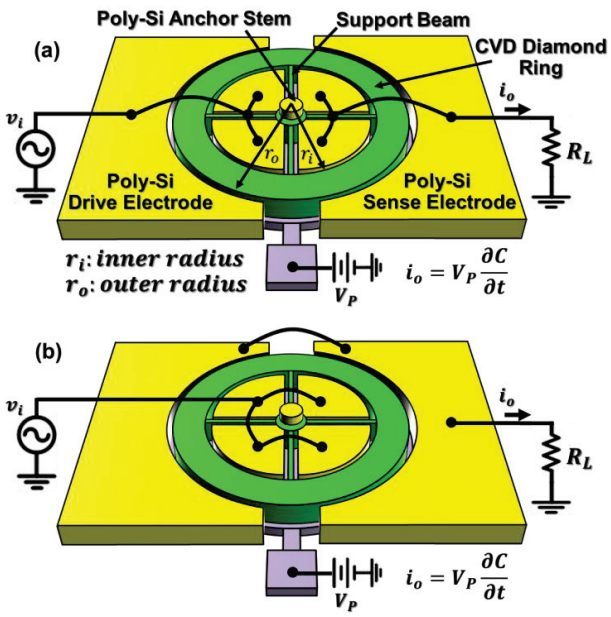

Fig. 2: Perspective views of ring resonators in typical two-port bias schemes for (a) electrode configuration A; and (b) electrode configuration B.

ring of [4] with hot filament CVD polycrystalline diamond structural material. Doing so yields record high Q's of 77,400 at 900MHz and 42,900 at 3GHz, the last of these posting an $f{\cdot}Q$ of $1.27{\times}10^{14}$, which is the highest to date among room-temperature acoustic devices.

II. Device Operation and Design

Fig. 2 presents perspective-view schematics of spoke-supported ring resonators using two different electrode configurations, both under typical two-port bias, excitation, and measurement schemes. As shown, each device consists of a boron doped micro-crystalline polydiamond ring with thickness t, inner radius r_i, and outer radius r_o, suspended by support beams that emanate from a stem self-aligned to be at the very center of the ring [4]. Both the inner and outer edges of the ring are surrounded by electrodes spaced by d_0 =75nm. To excite the device in either one of the two port configurations of Fig. 2, a bias voltage V_P is applied to the ring and an ac signal v_i to drive electrodes. These voltages produce an ac force between the electrode and the ring at the frequency of v_i, which if applied at the resonance frequency of the ring structure excites a resonant motion, with displacement amplitude amplified by the Q.

The extensional radial contour mode shapes can be derived from [7]:

$$\Re(r) = [AJ_1(pr) + BY_1(pr)] \tag{2}$$

where $\Re(r)$ is the radial modal displacement at location r, p is a frequency-dependent parameter to be specified later, J_1 is the first order Bessel function of the first kind, Y_1 is the first order Bessel function of the second kind, and A and B are design specific constants [7]. Fig. 3(a) presents a finite element simulation (FEM) of the fundamental radial contour

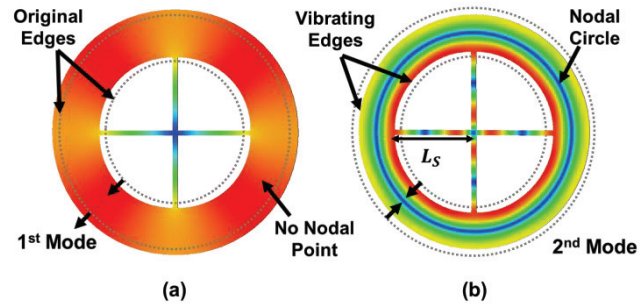

Fig. 3: Coventorware finite element simulations showing (a) the first radial contour mode, and (b) the second radial contour (or "breathing") mode.

mode shape in which red and blue represent maximum and minimum modal displacements, respectively. In this mode, the ring inner and outer radii expand and contract in phase, much like a disk with its center hollowed-out. Fig. 3(b) presents the second radial mode in which the inner and outer edges of the ring move in opposite directions, creating a so-called "breathing" mode that sports a nodal line between the ring edges. The support beams are made symmetric and balanced, c.f. Fig. 3, to cancel forces at the center of the ring thus minimizing transfer of motion to the stem and substrate. This work focuses on the second radial mode as it is most amenable to simultaneous high frequency and Q.

The ring resonance frequency is governed by [8]

$$\begin{aligned}&[J_1(pr_i)\sigma - J_1(pr_i) + r_i pJ_0(pr_i)] \\ &\qquad \times [Y_1(pr_o)\sigma - Y_1(pr_o) + r_o pY_0(pr_o)] \\ &-[Y_1(pr_i)\sigma - Y_1(pr_i) + r_i pY_0(pr_i)] \\ &\qquad \times [J_1(pr_o)\sigma - J_1(pr_o) + r_o pJ_0(pr_o)] = 0\end{aligned} \tag{3}$$

where σ is the Poisson ratio of the structural material. By solving (3) for the frequency parameter p, the resonance frequency is determined to be

$$f_0 = \frac{p}{2\pi}\sqrt{\frac{E}{\rho(1-\sigma^2)}} \tag{4}$$

where E is the Young's modulus of the structural material. The first and second solutions of (3) correspond to the mode shapes seen in Fig. 3(a) and 3(b), respectively.

While providing an exact frequency solution for all ring modes, equations (3) and (4) do not clearly convey the relationship between resonance frequency and design parameters. To make this relationship more obvious, equation (4) can be approximated for $r_i/r_o > 0.5$ by

$$f_{0/approx} = \frac{(m-1)}{2(r_o-r_i)}\sqrt{\frac{E}{\rho}},\ m = 2,3,4,\ldots \tag{5}$$

In this form, the strong dependence of resonance frequency on the width of the ring—a lateral dimension—is made clear. This dependence allows for multiple frequencies on a single-chip in a single lithography step, where multiple f_0's are specified only by CAD layout, marking one of the most compelling features of this technology when compared with traditional devices such as FBAR's. This is especially important for frequency processing systems targeted for future cognitive radio [9], such as RF channelizers that require

banks of many filters (e.g., hundreds) spanning a wide frequency range.

At resonance, the circuit behavior of this device is perhaps best described by the motional resistance R_x between its input and output electrodes, which gauges the amount of input voltage v_i needed to generate a given output current i_o. In this regard, the dc bias voltage V_P again plays a pivotal role, since the voltage across the time-varying output electrode-to-resonator capacitor strongly influences i_o. For the given excitation v_i, the motional impedance of the resonator is determined by [4]

$$R_x = \frac{v_i}{i_o} = \frac{d_0^4}{V_P^2 Q}\ \frac{1}{\omega_0 \varepsilon_0}\ \frac{1}{S} \tag{6}$$

where ε_0 is the vacuum permittivity, ω_0 is the angular resonance frequency, and S is a function of area and stiffness defined for the different electrode configurations of Fig. 2 as follows

$$S_A = \frac{A_{ro,d}A_{ro,s}}{k_{ro}} + \frac{A_{ro,s}A_{ri,d}}{k_{ri}}\frac{\Re(r_o)}{\Re(r_i)} + \frac{A_{ro,d}A_{ri,s}}{k_{ro}}\frac{\Re(r_i)}{\Re(r_o)} + \frac{A_{ri,d}A_{ri,s}}{k_{ri}} \tag{7a}$$

$$S_B = \frac{A_{ro,s}A_{ri,d}}{k_{ri}}\frac{\Re(r_o)}{\Re(r_i)} \tag{7b}$$

where (k_{ri}, k_{ro}), ($\Re(r_i)$, $\Re(r_o)$), and ($A_{ro,d}$, $A_{ri,d}$) are equivalent dynamic stiffness, modal displacements, and drive electrode (hence, *'d'* in subscripts) overlap areas at the inner and outer perimeters of the ring, respectively. $A_{ro,s}$ and $A_{ri,s}$ are similar parameters for the sense electrodes. Equation (6) clearly shows quadratic and linear reductions in R_x with increasing V_P and Q, respectively. Gap spacing d_0 commands an even stronger influence, where a decrease in d_0 yields a fourth power reduction in R_x.

III. Maximizing Resonator Q

To maximize the ring's Q, loss must be minimized. Among loss mechanisms that influence Q, material and anchor loss are often the most important at GHz frequencies. Material loss is generally governed by phonon-phonon interactions [5][6], which in turn depend upon acoustic velocity and thermal conductivity, where diamond's values of 18,500ms^{-1} and 2000Wm^{-1}K^{-1}, respectively, give it a (theoretical) advantage over many other materials at GHz frequencies. At least theoretically, with some dependence on what values are used for material constants, diamond is predicted to allow a maximum Q of 380,000 at 3GHz, to be compared with the 36,000 and 3,400 predicted for silicon and AlN, respectively [10].

Provided material loss theory can be trusted, anchor losses will likely govern the ultimate Q of this device. Like the design of [4], the ring of this work employs quarter-wavelength support beams to minimize escape of energy to the substrate. To expand on this, the support beam of Fig. 4(a) can be modeled by the T-network shown in Fig. 4(b),

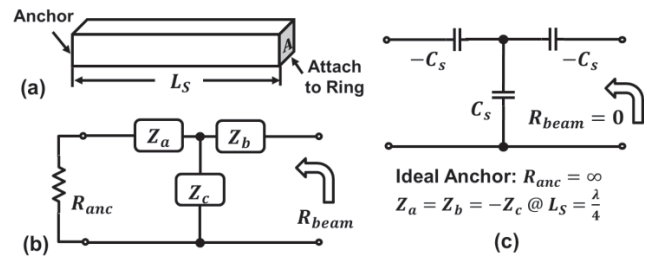

Fig. 4: (a) Perspective-view schematic of a support beam and (b) its equivalent T-network model. (c) The simplified T-network model for a quarter-wavelength support beam attached to an infinitely rigid anchor.

which mimics that used for electrical transmission lines. Here, R_{anc} gauges the acoustic energy loss to the substrate, and R_{beam} the acoustic loading of the beam seen by the ring. When the beam vibrates in an extensional mode, Z_a, Z_b, and Z_c take on values given by [11]

$$Z_a = Z_b = \frac{j}{Z_0}\tan\left(\frac{\alpha L_S}{2}\right) \text{ and } Z_c = \frac{1}{B} = \frac{-j}{Z_0 \sin(\alpha L_S)} \tag{8}$$

where L_S is the length of the support beam, Z_0=1/($A(\rho E)^{1/2}$) is the characteristic mobility, α=ω_o/v_e is the propagation constant, and v_e=$(E/\rho)^{1/2}$ is the material acoustic velocity.

The beam length corresponds to an effective quarter-wavelength when

$$L_S = \frac{n}{4f_0}\sqrt{E/\rho}\,,\ n = 1,3,5,\ldots \tag{9}$$

Substituting (9) into (8), the expressions for Z_a, Z_b, and Z_c then become

$$Z_a = Z_b = -Z_c = \frac{j}{Z_0} = \frac{k_{sa}}{j\omega} \quad \text{where } k_{sc} = -k_{sa} = 1/C_s = \omega_0 A\sqrt{\rho E} \tag{10}$$

Equation (10) converts the T-network to a pure capacitance network, as shown in Fig. 4(c). If the anchor is infinitely rigid, R_{anc} is infinite, and the effective capacitance of the beam seen by the ring becomes infinity. This makes R_{beam} zero, which allows the inner edge of the ring to move freely without resistance from the beam and with (ideally) zero energy transfer to it, thereby zero loss to the substrate.

The degree to which this ideal condition can be realized depends not only on how precisely dimensions can be set to quarter-wavelength specs, but also on the degree to which the anchors can be made infinitely rigid. To this point, the balanced symmetrical support structure of Fig. 3 is quite beneficial, since forces imposed by the beams on the anchor are always in phase, so cancel at the anchor, making the anchor appear extremely rigid.

To illustrate the importance of quarter-wavelength design, Fig. 5 presents FEM images generated using Coventorware for spoke-supported rings equipped with (a) quarter-wavelength (3λ/4 in this case) support beams and (b) non-quarter-wavelength (2.8λ/4) ones. As shown, the quarter-wavelength design of (a) clearly exhibits less mode distortion, so is freer to vibrate in the desired ring breathing mode and should yield higher Q in an actual implementation. Note that both designs benefit from the balanced symmetrical

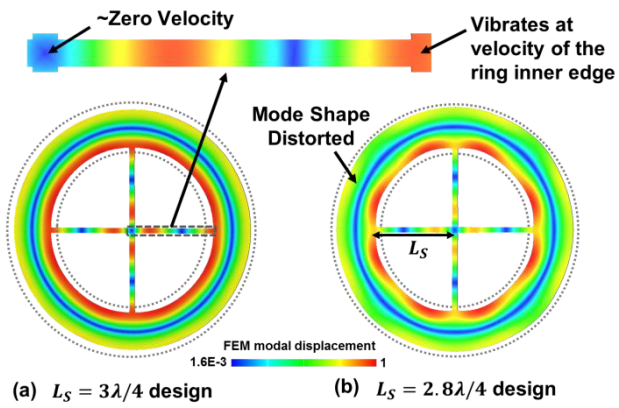

Fig. 5: Coventorware simulations comparing modal displacements when the supports are (a) quarter-wavelength and (b) non-quarter-wavelength.

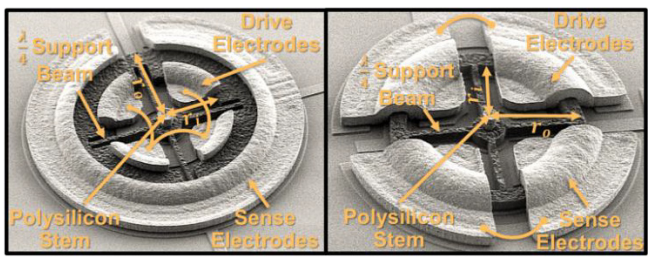

Fig. 6: SEM's of fabricated ring resonators: (a) a 900-MHz ring resonator using electrode configuration B; and (b) a 3-GHz ring resonator using electrode configuration A.

spoke-support structure, where the blue color of their anchors indicates minimal motion at the anchor, and thus, minimum loss to the substrate.

IV. Experimental Results

Spoke-supported rings at various frequencies were fabricated using a process flow practically identical to that used for the CVD polydiamond devices of [12]. Fig. 6(a) presents the SEM of a 900-MHz fabricated ring resonator using electrode configuration B, where the drive electrode combines the four inner electrodes, while the outer electrode surrounding the ring serves as the sense port. Fig. 6(b) presents the SEM of a 3-GHz fabricated ring resonator using electrode configuration A, where both drive and sense electrodes consist of two inner and two outer electrodes. The diamond ring is the darker material in Fig. 6. Although its surface looks rough, this material still yields remarkable Q's.

From (6), the motional resistance of a capacitive-gap transduced spoke-supported ring is inversely proportional to its frequency, so the devices of Fig. 6, even with 75nm gaps, are expected to exhibit high R_x's on the order of 60kΩ and 100kΩ for the 900-MHz and 3-GHz versions, respectively. (Note that if they had 20nm gaps, the R_x's would be 320Ω and 500Ω, respectively.) Although high, such resistances are actually still measurable using the direct measurement scheme depicted in Fig. 2, where the output current of a ring driven at resonance is directly sensed by an impedance-mismatched network analyzer. Indeed, the direct measurement scheme of Fig. 2 has been used successfully to characterize the performance of numerous high frequency, high impedance resonators [13][14], but only when they are equipped with ground planes and other strategies to suppress feedthrough currents that would otherwise mask the desired output current at the same frequency. Unfortunately, the devices of this work are not equipped with feedthrough suppressing mechanisms, and this renders the measurement scheme of Fig. 2 ineffective.

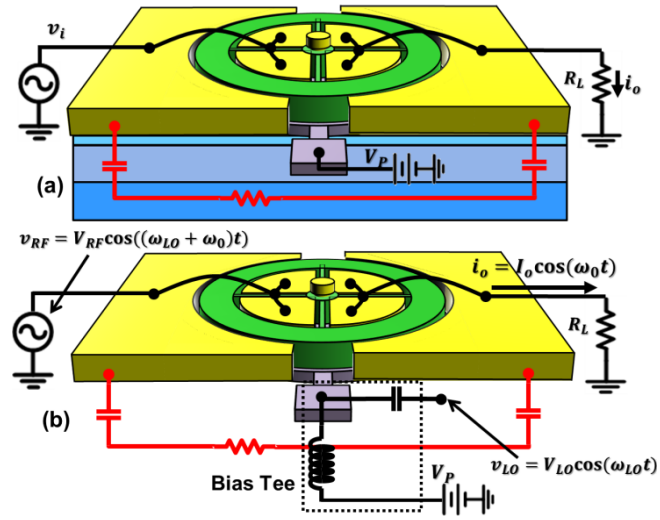

Fig. 7: Schematics comparing (a) a typical two-port measurement scheme with (b) the mixing measurement scheme used here, both showing the most troublesome parasitic feedthrough path for the fabricated devices.

To expand on this, Fig. 7(a) includes the substrate layers underlying a ring device, showing how the most troublesome path comprises the series connection of the static capacitors from device electrodes/bond pads to the substrate and the resistive path between those capacitors. The signal feeding through this path becomes especially severe as frequencies rise to the GHz range addressed, here.

A. Mixing Measurement Setup

To circumvent masking by feedthrough, this work employs the mixing measurement [15] setup, shown in Fig. 7(b), that essentially separates motional and feedthrough currents in the frequency domain, thereby allowing measurement of motional current without interference. As shown, this setup uses a bias tee to add a local oscillator signal to the dc-bias voltage already applied to the conductive resonator structure. An Agilent E5071B Network Analyzer then sources an RF signal at a frequency higher than the expected resonance frequency by the frequency of the local oscillator signal. Note that none of the applied signals are at the resonance frequency of the ring under test, so none of them can introduce feedthrough at this frequency. As long as a frequency domain detector is used, which is the case when a network analyzer senses the resonator output, parasitic feedthrough currents at frequencies different from the motional current cannot interfere with it.

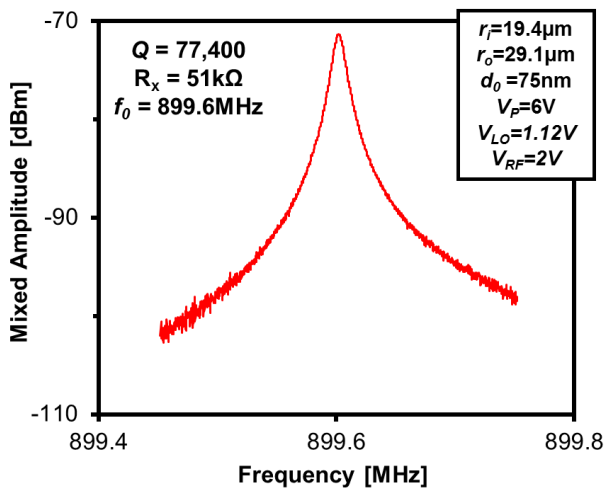

Fig. 8: Mixing-measured frequency response of the 900-MHz ring.

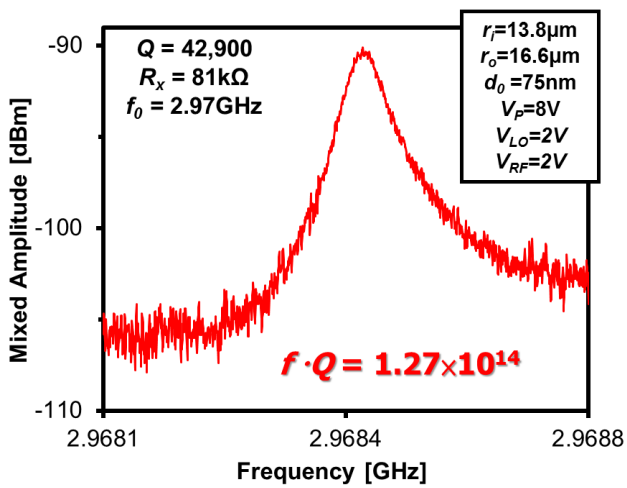

Fig. 9: Mixing-measured frequency response of the 3-GHz ring.

Even though none of the applied signals are at the resonance frequency f_0, they still generate a mechanical force at resonance via the square-law voltage-to-force transfer function of the input capacitive transducer, where

$$F = \frac{1}{2}\left(\frac{\partial C_i}{\partial r}\right)(V_P + V_{LO}\cos(\omega_{LO}t) - V_{RF}\cos(\omega_{RF}t))^2 \rightarrow$$
$$F = \frac{1}{2}\left(\frac{\partial C_i}{\partial r}\right)(V_P^2 + \cdots + 2V_{LO}V_{RF}\cos(\omega_{LO}t)\cos(\omega_{RF}t) + \cdots) \quad (11)$$

and where multiplication of the LO and RF signals generates a force at the resonance frequency:

$$F\,@\omega_0 = K \cdot V_{LO} \cdot V_{RF} \cdot \cos\left((\omega_{RF} - \omega_{LO})t\right) \rightarrow$$
$$F\,@\omega_0 = K \cdot V_{LO} \cdot V_{RF} \cdot \cos(\omega_0 t) \quad (12)$$

This forcing term allows the Agilent E5071B Network Analyzer operating in frequency offset mode to sense the resonant peak without interference from feed-through signals at ω_{RF} and ω_{LO}.

B. Experimental Results

Fig. 8 presents the mixed frequency response measured using the described mixing method for the 900-MHz diamond ring device of Fig. 6(a) operating in the second contour mode of Fig. 3(b). The inner and outer radii of this device are 19.4μm and 29.1μm, respectively, and the device is biased with V_P=6V during measurement. The measured center frequency is 889.6MHz, and the extracted motional resistance is 51kΩ, which is consistent with theoretical expectation. A Lorentzian fit to the response yields a measured Q of 77,400, which is the highest Q reported to date at this frequency for any room-temperature acoustic device.

Fig. 9 presents a similar mixed frequency response measurement for the 3-GHz diamond ring of Fig. 6(b) with inner and outer radii 13.8μm and 16.6μm, respectively. With bias voltage V_P of 8V, the measured center frequency is 2.97GHz, the extracted motional resistance is 81kΩ, and the Q is 42,900—yielding an $f{\cdot}Q$ product of 1.27×10^{14}, which is the highest reported value to date for any room-temperature acoustic resonator at any frequency. To illustrate the uniqueness of this device, Fig. 10 presents a graph of $f{\cdot}Q$ product versus device frequency comparing the $f{\cdot}Q$ products of previously published record-holding $f{\cdot}Q$ acoustic resonators along with those of this paper.

It should be noted that despite their similar motional resistances, the 3-GHz device frequency response peak is about 20dB lower than that of the 900-MHz device. The discrepancy comes from current loss at the higher frequency due to a large parasitic capacitance introduced by measurement system. This capacitance increases the impedance mismatch between the resonator motional resistance and the impedance seen into the network analyzer sense port, which is no longer purely resistive at the higher frequency.

C. Implications

For oscillators that limit in a way where Leeson's equation (i.e., (1)) holds, the measured Q's exceeding 77,000 in the GHz range should tremendously decrease phase noise. To illustrate, Fig. 11 presents hypothetical phase noise plots using Leeson's equation for 2-GHz oscillators employing resonators with Q's as measured in this work against curves based on actual measured phase noise for FBAR [17] and LC voltage-controlled (VCO) oscillators [18]. If the measured ring resonator were used in an oscillator while maintaining reasonable linearity, i.e., while keeping ring displacements less than 20% of the gap, the resulting oscillator would exhibit a close-to-carrier phase noise 41dB lower than the LC VCO, though its far-from-carrier phase noise would be higher by 17dB due to the lower power handling ability of the capacitive-gap transduced ring.

Of course, the above hypothetical oscillator could only be possible if an amplifier were available to instigate and sustain oscillation—a challenging proposition given the very large motional resistance of the device. From (6), reducing the electrode-to-resonator gap d_0 of the device would yield a considerably smaller motional resistance. For example, if the gap were reduced from 75nm to 30nm via the partial ALD gap filling method of [19], the close-to-carrier phase noise reduction over the LC VCO would rise to 52dB,

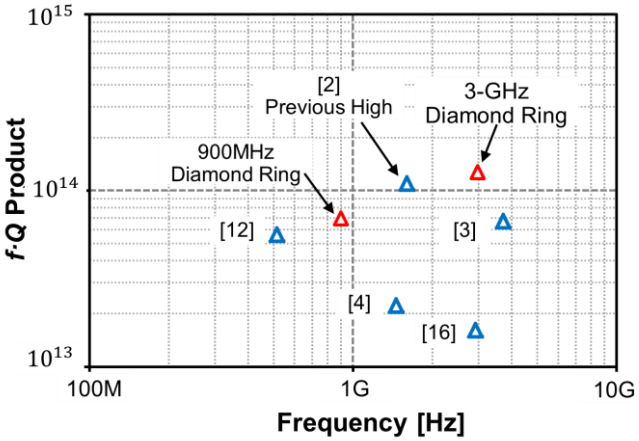

Fig. 10: The $f{\cdot}Q$ products of previously published record-holding high $f{\cdot}Q$ acoustic resonators along with those of this paper.

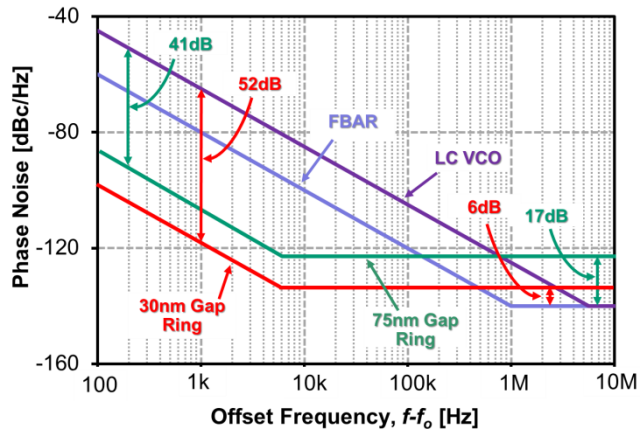

Fig. 11: Hypothetical phase noise plots of different oscillators using Leeson's equation. The FBAR and VCO plots are derived from actual measurements in [17] and [18], respectively.

and the far-from-carrier phase noise shortfall would shrink to 6dB, as shown in Fig. 11. This deficit could easily be overcome by arraying, as demonstrated in [20].

V. Conclusion

CVD diamond ring resonators with balanced symmetrical quarter-wavelength support beams designed to suppress anchor loss, have achieved record high Q's of 77,400 at 900MHz and 42,900 at 3GHz, the latter of which marks the highest $f{\cdot}Q$ of $1.27{\times}10^{14}$ yet reported among room-temperature acoustic devices. The motional impedance of these devices are somewhat high, but can be greatly reduced by partial ALD gap filling and arraying resonators—both of which have been demonstrated in similar devices in the recent past. If and when such resistance-lowering methods are successful, the CAD-definable resonance frequencies dependent mainly on lateral dimensions and record-setting Q's demonstrated by the CVD polydiamond ring devices of this work might be ideal for realization of the single chip RF channel-select filters and low phase noise oscillators targeted for future compact mobile communications, including those aimed at software-defined cognitive radio [9].

References

[1] D.B. Leeson, "A simple model of feedback oscillator noise spectrum," *Proc. IEEE*, vol.54, no.2, pp. 329- 330, Feb. 1966.

[2] G. R. Kline, K. M. Lakin, and K. T. McCarron, "Overmoded high Q resonators for microwave oscillators," in *Proc. IEEE Int. Frequency Control Symposium*, 1993, pp. 718 –721.

[3] E. Hwang and S. A. Bhave, "Transduction of High-Freq. Micromechanical Resonators Using Depletion Forces in p-n Diodes," *IEEE Trans. on Electron Devices*, vol. 58, no. 8, pp. 2770 –2776, Aug. 2011.

[4] S.-S. Li, Y.-W. Lin, Y. Xie, Z. Ren, and C. T.-C. Nguyen, "Micromechanical 'hollow-disk' ring resonators," in *Proc. IEEE Int. Micro Electro Mechanical Systems, 2004*, 2004, pp. 821 – 824.

[5] R. Tabrizian, *et al.*, "Effect of phonon interactions on limiting the f.Q product of micromechanical resonators," in *IEEE Int. Conf. on Solid-State Sensors, Actuators (Transducer '09).* pp. 2131 –2134.

[6] V.B. Braginsky, *et al.*, System with Small Dissipation, The University of Chicago Press, 1985.

[7] A. Iula, *et al.*, "A model for the theoretical characterization of thin piezoceramic rings," *IEEE Trans. Ultrasonics, Ferroelectrics and Frequency Control,* vol.43, no.3, pp. 370 –375, May 1996.

[8] C. V. Stephenson, "Radial vibrations in short, hollow cylinders of Barium Titanate," *J. Acoust. Soc. Amer.,* vol.28, no.1, pp.51-56, Jan. 1956.

[9] C. T.-C. Nguyen, "Integrated micromechanical RF circuits for software-defined cognitive radio (invited plenary*)," Proceedings, the 26th Symposium on Sensors, Micromachines & Applied Systems, Tokyo, Japan*, Oct. 15-16, 2009, pp. 1-5.

[10] M. Akgul, *et al*, "Hot filament CVD conductive microcrystalline diamond for high Q, high acoustic velocity micromechanical resonators," in *IEEE Int. IFCS-EFTF*, 2011, pp. 1-6.

[11] R. A. Johnson, *Mechanical Filters in Electronics*. New York, NY: Wiley, 1983.

[12] T. O. Rocheleau, T. L. Naing, Z. Ren, and C. T.-C. Nguyen, "Acoustic whispering gallery mode resonator with Q >109,000 at 515MHz*," in IEEE Int. Conf. on MEMS,* 2012, pp. 672 –675.

[13] J. Wang, Z. Ren, and C. T.-C. Nguyen, "1.156-GHz self-aligned vibrating micromechanical disk resonator," *IEEE Trans. UFFC,* vol. 51, no. 12, pp. 1607 –1628, Dec. 2004.

[14] J. R. Clark, *et al.*, "High-Q UHF micromechanical radial-contour mode disk resonators," *J. Microelectromechanical Systems,* vol.14, no.6, pp. 1298- 1310, Dec. 2005.

[15] A.-C. Wong and C. T.-C. Nguyen, "Micromechanical mixer-filters ('mixlers')," *J. Microelectromechanical Systems,* vol. 13, no. 1, pp. 100 – 112, Feb. 2004.

[16] C.-M. Lin, *et al.*, "AlN/3C-SiC composite plate enabling high-frequency and high-Q micromechanical resonators," *Adv. Mater.*, vol. 24, no. 20, pp. 2722-2727, May 2012.

[17] A. Nelson, J. Hu, J. Kaitila, R. Ruby, and B. Otis, "A 22µW, 2.0GHz FBAR oscillator," in *Radio Frequency Integrated Circuits Symposium (RFIC)*, 2011 IEEE, 2011, pp. 1 –4.

[18] H. Kim, *et al.*, "A Low Phase Noise LC VCO in 65 nm CMOS Process Using Rectangular Switching Technique," *IEEE Lett. Microwave and Wireless Components*, vol. 17, no. 8, pp. 610 –612, Aug. 2007.

[19] M. Akgul, B. Kim, Z. Ren, and C. T.-C. Nguyen, "Capacitively transduced micromech. resonators w/ simultaneous low motional resistance and Q>70,000," *Proc., Hilton-Head Conf.*, Jun. 2010, pp.467-470.

[20] Y.-W. Lin, S.-S. Li, Z. Ren, and C. T. C. Nguyen, "Low phase noise array-composite micromechanical wine-glass disk oscillator," in *IEEE Int. Tech. Dig., Electron Devices Meeting*, 2005., pp. 287-290.